Minimum enstrophy principle for two-dimensional inviscid flows around obstacles

F. Muller, A. Burbeau, B.-J. Gréa, Pierre Sagaut

Minimum enstrophy principle for two-dimensional inviscid flows around obstacles

F. Muller* and A. Burbeau
CEA Saclay, DEN, DM2S/STMF, F-91191 Gif/Yvette, France

B.-J. Gréa
CEA, DAM, DIF, F-91297 Arpajon, France

P. Sagaut
Aix Marseille Univ, CNRS, Centrale Marseille, M2P2 UMR 7340, 13451 Marseille, France

(Received 1 August 2018; published 11 February 2019)

Large-scale coherent structures emerging in two-dimensional flows can be predicted from statistical physics inspired methods consisting in minimizing the global enstrophy while conserving the total energy and circulation in the Euler equations. In many situations, solid obstacles inside the domain may also constrain the flow and have to be accounted for via a minimum enstrophy principle. In this work, we detail this extended variational formulation and its numerical resolution. It is shown from applications to complex geometries containing multiple circular obstacles that the number of solutions is enhanced, allowing many possibilities of bifurcations for the large-scale structures. These phase change phenomena can explain the downstream recombinations of the flow in rod-bundle experiments and simulations.

DOI: 10.1103/PhysRevE.99.023105

I. INTRODUCTION

In nearly two-dimensional turbulent flows, the inverse cascade process, transferring energy from smaller scales to larger ones, is responsible for the formation and the growth of large-scale coherent structures. Predicting their stability and dynamics is fundamental in a wide array of fields, from oceanic and atmospheric thin layers to astrophysical phenomena. The Great Red Spot in the Jupiter atmosphere [1], or the intermittent behavior of the Kuroshio current in the Pacific ocean [2] are well-known examples among many others.

In this context, statistical fluid mechanics have proved a valuable tool for analyzing these phenomena. A crucial part of the study of two-dimensional (2D) flows is the prediction of the steady stable structures emerging from given initial characteristics and depending on the domain geometry. Instead of an exhaustive application of a dynamical stability criterion to the infinite set of steady solutions to the Euler equations, an equivalence is used between such a dynamical stability criterion and a constrained optimization problem, usually on a measure of the entropy with conservation of a varying set of Euler invariants. This allows for the use of several tools coming from mathematical optimization theory, and to directly calculate the expected steady state in a given 2D physical configuration.

From the work of Onsager [3] on a point vortices model followed by the Joyce-Montgomery theory [4] to the energy-enstrophy Kraichnan theory [5,6] as well as the Miller-Robert-Sommeria theory [7,8], various methods have been proposed in order to construct a variational problem allowing the determination of steady stable states. Among this variety, the minimum-enstrophy-principle (MEP) has been very popular partly due to its simplicity. This principle was initially proposed through phenomenological considerations based on a so-called *selective decay process* by Bretherton and Haidvogel [9], Matthaeus and Montgomery [10], and Leith [11]. Under this justification, the MEP assumes that, while the total energy and circulation of the flow are relatively well conserved, the enstrophy (the second moment of the vorticity) is dissipated down to a hypothetical minimum value associated with the steady stable state, leading to a doubly-constrained minimization problem on the enstrophy. The MEP is particularly useful for the explicit determination of steady stable states as it leads to a linear relationship between vorticity and stream function, which greatly simplifies the underlying calculations. It was notably used to identify stable steady states and geometry-induced bifurcations by Naso *et al.* [12,13].

The more general theory developed by Miller, Robert, and Sommeria [7,8] (MRS) uses the maximization of the entropy under the conservation of all Euler invariants to determine stable states. The MEP can be related to a low-energy limit case of the MRS theory as discussed by Chavanis and Sommeria [14]. Beyond its initial phenomenological justification, it was also shown by Naso *et al.* [12] that the MEP (minimization of the enstrophy at fixed energy and circulation) is equivalent to a maximization of the entropy at fixed energy, circulation, and microscopic enstrophy. This equivalence constitutes a justification of the MEP from statistical mechanics, which substantiates its validity further than sole phenomenological considerations. Other possible variational problems have been proposed [12,15] and relationships between the various approaches were discussed by Chavanis [16] and Bouchet [17]. Existing studies are most of the time performed through

*florian.muller@cea.fr

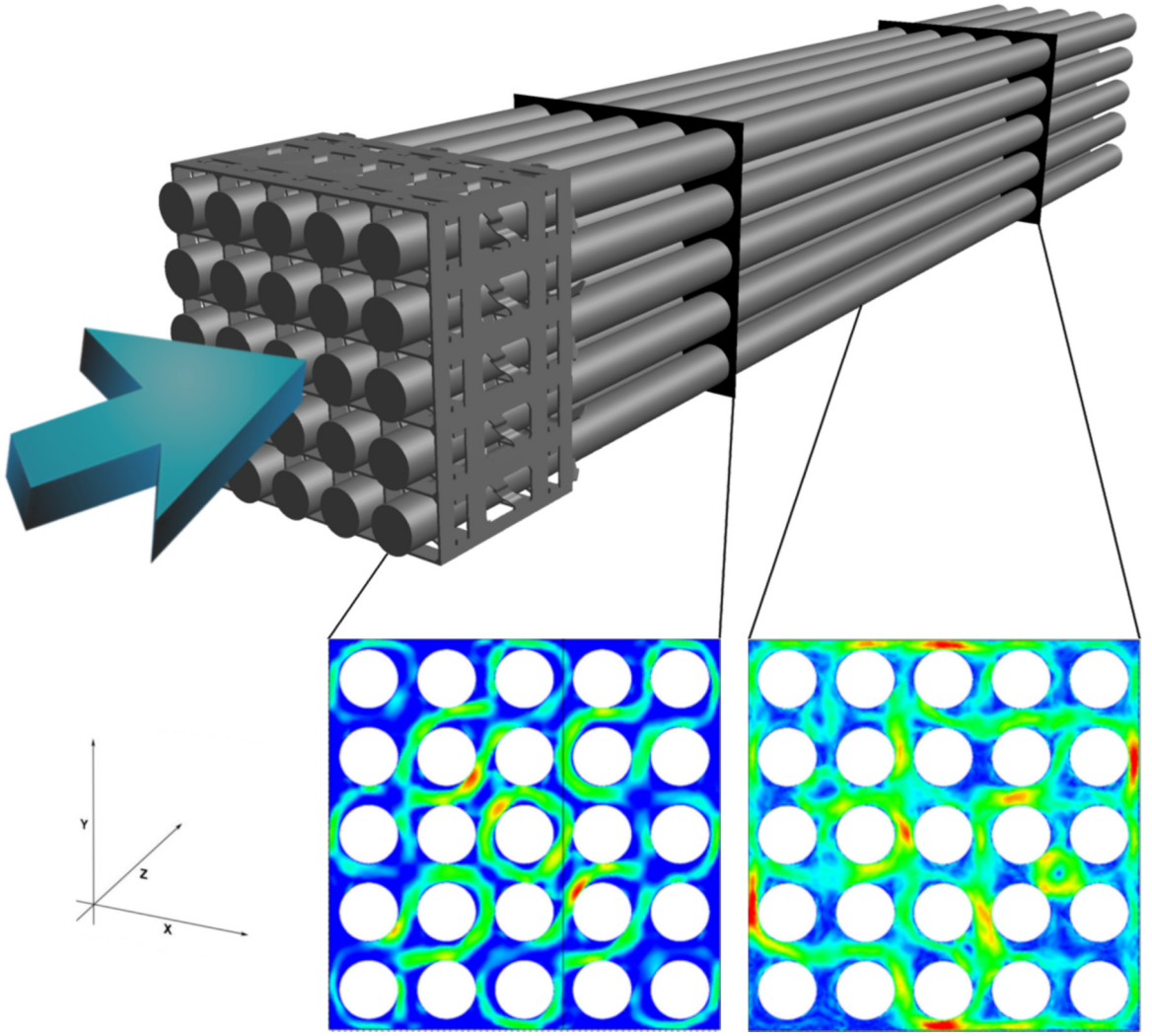

FIG. 1. Sketch of the tranvserse flow fields observed in cross sections of an experimental 5×5 rod-bundle flow after the passage of the coolant flow in the interstices between a mixing grid and the cylinder array. The flow is injected with a mostly axial velocity field as depicted by the bottom-left arrow. The cross sections of the flow shown here are respectively found at axial positions $z = 3.4d_h$ (left) and $34d_h$ (right) away from the grid. While cropped here for visibility, the cylinders extend from far upstream of the mixing grid until its far wake downstream.

an analytical approach, with a direct derivation of the solutions from the variational maximization of the entropy. The typically considered domain geometries, namely, the square, rectangle, and disk, are devoid of internal obstacles.

In this work, we propose to apply statistical fluid mechanics methods to flows constrained by more complex geometries such as fuel rod bundles in a pressurized-water reactor (PWR). A rod bundle basically consists of an array of parallel cylinders, placed within a container of usually square section, and maintained together by regularly spaced grids as represented in Fig. 1. A coolant flow is injected at one extremity of the bundle, and its velocity field is mostly aligned with the cylinder axes. Mixing vanes are added to the spacer grids in the interstices between the cylinders in order to increase interchannel velocities in transverse planes orthogonal to the rod axes and thus enhance the thermal mixing of the flow. Just as in the case of 2D inviscid flows, steady coherent structures appearing in these transverse flows (as seen in Fig. 1) experience reorganization phenomena which we wish to interpret as phase transitions in the sense of statistical physics. Examples of such reorganizations are the large-scale rotation of the flow described in Bieder *et al.* [18] or the intercylinder velocity inversion described in Shen *et al.* [19].

A better understanding of this secondary transverse flow is paramount in the process of PWR safety analyses. However, it has proved difficult to study it using purely computational fluid dynamics (CFD) -based approaches, as indeed the high Reynolds number ($R_e \simeq 10^5$) and the large spatial size of the system drive the computational costs of a well-resolved simulation to quite prohibitive values. As such, we aim to advance a methodology for the study of this type of flow, namely, the usage of tools from inviscid two-dimensional statistical fluid mechanics, in addition to three-dimensional CFD simulations.

At first glance, statistical fluid dynamics do not apply to this three-dimensional flow. However, one can observe that the streamwise mean velocity U_z (i) is usually much larger than its crosswise part $\mathbf{u}_{x,y} \ll U_z$ and (ii) weakly depends on spatial coordinates. As a consequence and as a first approximation, the crosswise mean velocity field is simply advected by the

streamwise mean part. This corresponds to the Taylor frozen turbulence hypothesis which is thus applied to the secondary flow field $\mathbf{u}_{x,y}$ in order to correlate the axial coordinate of a three-dimensional (3D) flow section to the time variable and the bulk axial velocity. The total velocity field can be decomposed as

$$\mathbf{U}(x, y, z, t) = U_z \mathbf{e}_z + \mathbf{u}_{\mathbf{x},\mathbf{y}}(x, y, U_z t) + \mathbf{u}'(x, y, z, t) \quad (1)$$

with U_z the axial velocity nearly uniform in the bulk of the flow, $\mathbf{u}_{\mathbf{x},\mathbf{y}}(x, y, U_z t)$ the transverse flow field to which is applied the Taylor "frozen turbulence" hypothesis leading to a correlation $z = U_z t$, and $\mathbf{u}'(x, y, z, t)$ the 3D turbulent fluctuations. Notably, the boundary layers in the physical setup of PWR rod-bundle flows were observed to be quite thin due to the high Reynolds number and were free of detachments, which we use as a justification to place our study exclusively in the *bulk* of the flow. Therefore, we can apply inviscid 2D statistical fluid mechanics to the "transported" two-dimensional transverse mean bulk flow field.

Accordingly, these tools must be adapted as a first step to more complex geometries, notably through the consideration of one and possibly multiple obstacles. Nonconnex boundaries bring forth an additional complexity to the problem through a larger set of possible Dirichlet boundary conditions for the optimization problem, which has been sparsely explored in the existing literature. An annular geometry was considered by Corvellec [20] and Chen and Cross [21], but using a resolution method specifically tailored for a ring-shaped domain geometry. In this study, we aim at presenting an adaptation of the MEP to domains containing obstacles. This will be achieved through the inclusion of an additional equation in the standard optimization problem, the discretization of the usually analytical method, and a parametric exploration method of the parameter space, in order to allow the identification of stable steady states thanks to the minimum enstrophy principle. Eventually our goal is to pave the way for a concrete utilization of this type of resolution methods in the field of rod-bundle flow thermohydraulics.

The governing theory and equations of our study are displayed in Sec. II, and our method for explicitly obtaining solutions and exploring the parameter space is given in Sev. III. Validation results for the method are presented in Appendix C, and results obtained in the simple case of a ring are shown in Sec. IV. At last, the capability of the method to handle domain geometries with a higher number of obstacles is assessed in Sec. V.

II. THEORETICAL FRAMEWORK: MINIMUM-ENSTROPHY STATES

Considering the case of a two-dimensional inviscid fluid system, we first address the two-dimensional vorticity equations (derived from the incompressible Euler equations) written as

$$\begin{aligned} \frac{\partial \omega}{\partial t} + \mathbf{u} \cdot \nabla \omega = 0, \\ \omega \mathbf{z} = \nabla \times \mathbf{u}, \end{aligned} \quad (2)$$

where ω is the vorticity, $\mathbf{u}$ the velocity field, and $\mathbf{z}$ a unit vector normal to the flow. Let ψ be the stream function defined as

$$-\Delta \psi = \omega. \quad (3)$$

The 2D Euler equations admit an infinite number of steady states of the form $\omega = f(\psi)$ where f is an arbitrary function. These solutions are obtained by solving

$$\begin{aligned} -\Delta \psi = f(\psi) = \omega, \\ \psi = a \in \mathbb{R}, \quad \text{on the domain boundary.} \end{aligned} \quad (4)$$

Among the infinite set of steady solution states to problem (4), it must be noted that a vast majority are unstable. and are unlikely to be observed.

In the case of the two-dimensional transverse flow fields studied in PWR rod bundles using a Taylor "frozen turbulence" hypothesis, we hope to be able to draw interesting comparisons between 2D-predicted steady stable states in a rod-bundle cross-section geometry and coherent structures identified in transverse planes from actual 3D experiments or numerical simulations.

A classical stability criterion for the Euler equations is the sufficient Kelvin-Arnol'd energy principle [22,23], under which a flow that is an extremum of the energy under isovortical turbulent fluctuations (i.e., that amounts to a pure advection of vorticity) is dynamically stable. Various other stability criteria have been devised over the years, often through the optimization of a certain functional of the flow under a given set of constraints. As a rule of thumb, highly constrained approaches entail a relatively high degree of confidence in the thermodynamical stability of their solutions but are complex to use, while optimization criteria with a limited number of constraints are easier to enforce but cannot provide definite information on the flow stability. The mutual relationships within the set of optimization principles available is discussed in the literature, notably by Chavanis [16].

As mentioned in the Introduction and following Naso *et al.* [12], we choose to rely on the MEP in our study. We justify this choice of variational problem through the phenomenological argument of a small viscosity in real flows, leading to a relative conservation of both total energy and circulation but a strong decay of the macroscopic enstrophy until the latter eventually reaches a minimum value. This process was coined as a *selective decay*, where the system is supposed to spontaneously "pick" a state minimizing the macroscopic enstrophy for its long-time decay. Although such a justification is quite limited (see Brands *et al.* [24]), we deem it to render the MEP an interesting compromise between relevant steady-state solutions, relatively simple implementation, and relevance in real flow cases where a small but non-negligible viscosity is present, which is bound to be the case in our industry-aimed study. As it will appear in the analytic developments thereafter, the MEP approach has also the advantage of implying a linear relationship $\overline{\omega} - \overline{\psi}$, which greatly simplifies the numerical usage of this theory and the exploration of domain geometries with obstacles.

The selective decay principle, leading to the minimization of the enstrophy under conservation of the energy and circulation, can also be derived as a result of a *coarse-graining* process. Indeed, only the large-scale part of high-Reynolds

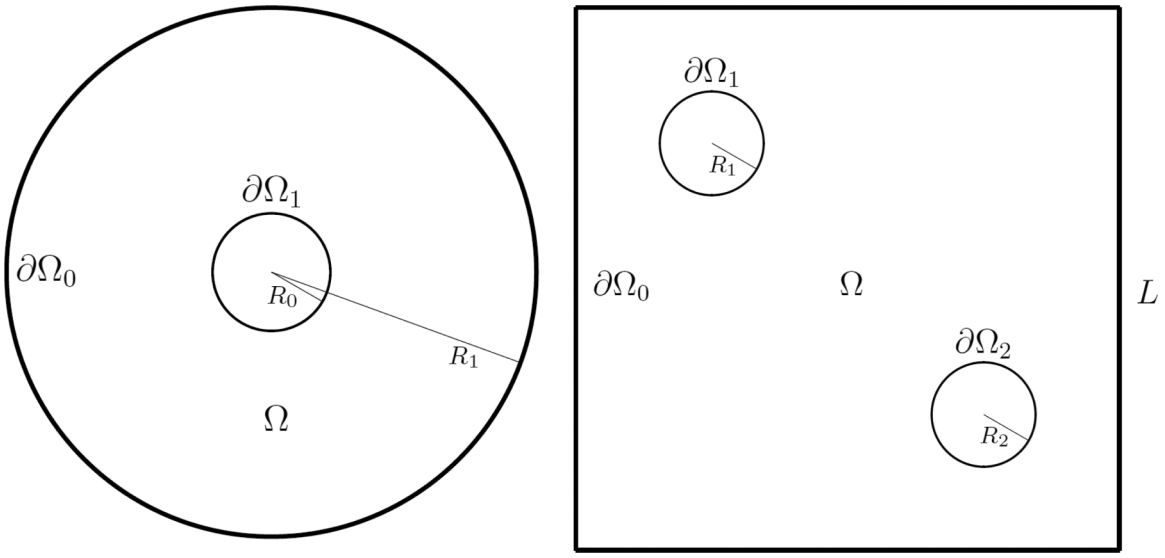

FIG. 2. Sketch of the two domain geometries explored in this study: a circular annulus domain (left) with $R_0 = 0.45$ and $R_1 = 0.1$, and a square with two obstacles (right) of side length $L = 1$ and obstacle radii $R_1 = R_2 = 0.1$.

turbulent flows are considered in practice. A coarse-graining process enables the separation between a *macroscopic* local average ($\overline{\omega}$ in the case of the vorticity) and small scales that are out of reach in a numerical approach. These two quantities are linked by a density probability function ρ containing the probability $\rho(\mathbf{r}, \sigma)$ to observe a vorticity level $\omega = \sigma$ at the spatial point $\mathbf{r}$. A consequence of this restriction to the large scales of an *inviscid* flow is the emergence of a hierarchy between the invariants. The total energy and circulation can be directly expressed as functions of the coarse-grained vorticity through ρ, implying their relative conservation. On the contrary, the second moment of the macroscopic vorticity, which is the macroscopic enstrophy $\Gamma_2^{\text{mac}} = \int \overline{\omega}^2 \mathbf{r}$, is inferior by Schwartz inequality to the microscopic enstrophy $\Gamma_2^{\text{mic}} = \int \overline{\omega^2} \mathbf{r}$ and is poorly conserved (which can be interpreted as small-scale fluctuations dissipating enstrophy much more efficiently than energy or circulation). The further higher-order Euler invariants can be treated with the same reasoning, leading to an even poorer conservation in the coarse-graining process; they are not considered invariants at all in this method. The variational principle stemming from the coarse-graining process is thus the MEP minimization of the macroscopic enstrophy with constraints on the total energy and circulation. This principle being applied *after* the coarse-graining process, it uses the macroscopic vorticity $\overline{\omega}$ as a variable, which greatly simplifies the implementation of the method, as in practice the explicit filter from the flow characteristics to their coarse-grained part does not need to be determined.

The more general MRS theory [7,8] transferred the problematic from steady states dynamical stability to the maximization of a mixing entropy under conservation of all quantities invariant under the Euler equations. It uses the density probability function ρ as the variable. The resulting multiply-constrained optimization problem is exhaustive but difficult to justify for real flows and to use in practice. As already mentioned, the MEP variational problem can be recovered as a limit case of the MRS theory for low-energy systems (see Chavanis *et al.* [14]); it leads to a sufficient MRS stability condition, which would allow us to find a certain ensemble of MRS-stable steady states but not all of them. Indeed, due to *ensemble inequivalence*, some MRS-stable states could only be "saddle" points in the MEP approach. We consider this restriction acceptable in our case, the aim being in a first step to identify possible stable steady states and draw comparisons between them and states observed in simple freely decaying 2D turbulent simulations.

It can be mentioned that the MEP is also equivalent to the Ellis-Haven-Turkington approach in the case of a Gaussian prior vorticity distribution as described by Ellis *et al.* [15], Chavanis [25], and Chavanis *et al.* [26].

In the following, solutions to problem (4) are searched after applying the coarse-graining process, although without explicitly considering the characteristics of the coarse-graining filter. We set the resolution in an abstract Ω domain with internal obstacles meant to be representative of the geometry of a fuel assembly cross section.

As illustrated in Fig. 2 for both $Q = 1$ and $Q = 2$, let Ω be a bounded polygon of $\mathbb{R}^2$ with a boundary named $\partial\Omega$. We place Q obstacles within the domain, $Q \geqslant 0$. Let $\partial\Omega_0$ be the exterior boundary of Ω and let $\partial\Omega_q$ with $q \in [1, Q]$ be an interior boundary of Ω, so that $\partial\Omega = \partial\Omega_0 \cup_{q\in[1,Q]} \partial\Omega_q$.

The solution ψ satisfies (to simplify the notation the $\bar{\cdot}$ is omitted)

$$\begin{aligned} -\Delta\psi &= \omega, \ \Omega \\ \psi &= a_q, \ \partial\Omega_q, \quad q \in [0, Q]. \end{aligned} \tag{5}$$

Excluding boundary layers in our study, slip boundaries are used in the following resolution. This translates to a simple impermeability condition for the fluid at a boundary $\partial\Omega$, which in turn imposes that $\mathbf{u} \cdot \mathbf{n} = \mathbf{0}$, with $\mathbf{n}$ a normalized vector normal to the boundary $\partial\Omega$. This leads to $\nabla\psi \times \mathbf{n} = 0$, meaning that ψ must have a constant value on each piece of boundary $\partial\Omega_q$. Since ψ is determined up to an arbitrary constant, we can assume without loss of generality that $a_0 = 0$.

Let us introduce the averaging operator $\langle\cdot\rangle$ on Ω:

$$\langle X\rangle = \int_\Omega X\, d\mathbf{r}. \tag{6}$$

The enstrophy, the circulation, and the energy are respectively defined as functions of the variable ψ as

$$\Gamma_2[\psi] = \frac{1}{2}\langle\Delta\psi\Delta\psi\rangle, \tag{7}$$

$$\Gamma[\psi] = -\langle\Delta\psi\rangle = -\int_{\partial\Omega}\nabla\psi\cdot\mathbf{n}\, d\sigma, \tag{8}$$

$$E[\psi] = \frac{1}{2}\langle\nabla\psi\nabla\psi\rangle. \tag{9}$$

Note that the factor $1/2$ in the definition of Γ_2 is arbitrary; we choose to use it in order to follow the framework set by Naso *et al.* [12]. However, the quantity $S = -1/2\langle\Delta\psi\Delta\psi\rangle$ is studied therein but we choose to omit the minus sign in order to remain on a minimization problem (following the MEP) rather than a maximization one.

The total circulation can be developed as

$$\Gamma = \sum_{q=0}^{Q}\Gamma_q = \sum_{q=0}^{Q}\oint_{\partial\Omega_q}\nabla\psi\cdot\mathbf{n}\, d\sigma. \tag{10}$$

As explained by Naso *et al.* [12], a dynamically stable solution in the sense of the MEP is a solution of the variational problem

$$\min_\psi\{\Gamma_2[\psi]|E[\psi] = E, \Gamma[\psi] = \Gamma\}, \tag{11}$$

which amounts to the enstrophy minimization while conserving the total energy E and the total circulation Γ. The Lagrange multipliers β and α are introduced in order to find the minimum of the enstrophy under these constraints. Let the Lagrange functional be defined in our problem as

$$J[\psi] = \Gamma_2[\psi] - \beta\left(\tfrac{1}{2}\langle\nabla\psi\cdot\nabla\psi\rangle - E\right) - \alpha(-\langle\Delta\psi\rangle - \Gamma). \tag{12}$$

A perturbation $\psi + \theta\phi$ with $\phi|_{\partial\Omega} = 0$ is introduced in order to obtain a variational form for J:

$$\begin{aligned} J[\psi+\theta\phi] = J[\psi] &- \theta\langle\Delta\psi\Delta\phi\rangle - \tfrac{1}{2}\theta^2\langle\Delta\phi\Delta\phi\rangle \\ &- \beta\theta\langle\nabla\psi\cdot\nabla\phi\rangle - \tfrac{1}{2}\beta\theta^2\langle\nabla\phi\cdot\nabla\phi\rangle + \alpha\theta\langle\Delta\phi\rangle. \end{aligned} \tag{13}$$

An extremum of J is obtained for a solution ψ verifying $\forall\phi$ at the first order in θ,

$$-\langle\Delta\psi\Delta\phi\rangle - \beta\langle\nabla\psi\cdot\nabla\phi\rangle + \alpha\langle\Delta\phi\rangle = 0. \tag{14}$$

Using an integration by parts on $\langle\nabla\psi\cdot\nabla\phi\rangle$, the boundary conditions $\psi = a_q$ on $\partial\Omega_q$, $q\in[0, Q]$, Eq. (14) translates $\forall\phi$ to

$$\langle(-\Delta\psi + \beta\psi + \alpha)\Delta\phi\rangle - \sum_{q=0}^{Q}\beta a_q\oint_{\partial\Omega_q}\nabla\phi\cdot\mathbf{n}\, d\sigma = 0. \tag{15}$$

If we restrict the range of the ϕ perturbations to those verifying $\nabla\phi\cdot\mathbf{n} = 0$ on $\partial\Omega$, we obtain the local problem satisfied by the solution ψ (11):

$$\Delta\psi = \beta\psi + \alpha = -\omega. \tag{16}$$

It should be noted in relation (16) that, as mentioned in Sec. I, the optimization problem (11) has indeed led to a linear $\omega - \psi$ relationship. We can take the space integral of (16) on Ω giving

$$\int_\Omega\Delta\psi\, d\mathbf{r} - \beta\int_\Omega\psi\, d\mathbf{r} = \alpha\int_\Omega 1\, d\mathbf{r}, \tag{17}$$

which when using the averaging operator defined in (6) leads to

$$\alpha = \langle\Delta\psi\rangle - \beta\langle\psi\rangle = -\Gamma - \beta\langle\psi\rangle. \tag{18}$$

Finally, expression (16) is used to isolate α, which leads to the fundamental equation to be solved:

$$-\Delta\psi + \beta\psi = \Gamma + \beta\langle\psi\rangle. \tag{19}$$

From (15), it appears that in order to obtain a dynamically stable state under the MEP, the following condition must also be fulfilled by the Lagrange multiplier β and the boundary conditions a_q for $q\in[0, Q]$:

$$\beta a_q = 0, \quad q\in[0, Q]. \tag{20}$$

The overall system to be solved by a solution ψ is (19),(20).

It should be noted that the criterion (20) is compatible with previous research on the subject, in particular [12,14]. Indeed, the common assumption of $a_0 = 0$ in cases with a single piece of boundary ensures the validity of (20). In cases with multiple pieces of boundary, (20) can be verified both through $a_q = 0$ or $\beta = 0$. Contrary to the single-boundary case, $\beta = 0$ does not necessarily lead to a zero-energy state thanks to the boundary terms as shown in the expression of the energy in (A7). This pair of possible solutions to (20) constitutes an expansion on the previously available ensemble of stable solutions ψ. As will be shown in the results in Sec. V, this expansion allows for notable bifurcations between stable solution patterns.

In Eq. (19), the constraints set on the optimization problem (11) are transferred as follows:

(1) the value of the circulation is explicitly present in Eq. (19);

(2) the energy constraint is transferred to the Lagrange multiplier β, which will be an essential variable in the following phase diagrams;

(3) the boundary condition a_q on ψ for each piece of boundary Ω_q is also impacted by the energy condition, since the expression of the energy now depends on a_q as detailed in Appendix A.

A solution ψ obtained through the resolution of Eqs. (19) and (20) with appropriate values for the constraints on the total energy and circulation will be by construction an extremum of the function $J[\psi]$. A further comparison of the enstrophy of the various possible extrema will deliver the minimum-enstrophy state, which under the MEP is a steady dynamically stable solution of the Euler equations. We will show that multiple stable states with equal values for the Euler invariants but for different boundary conditions and thus with

different circulations around the obstacles Γ_q can be obtained. Our interest being in the resolution of this problem in any given geometry with internal obstacles for a wide range of energy and total circulation values, we opted for a numerical resolution.

III. RESOLUTION METHOD

A. Direct expression of the solutions

The resolution method in the case of homogeneous boundary conditions follows the method developed by Chavanis *et al.* [14] and Naso *et al.* [12]. In this part, we extend the method to the case of nonhomogeneous boundary conditions but it is implemented first in a calculation tool and validated on simple geometries without internal obstacles, recovering the results presented in [12,14].

Following these studies, we regroup energy and circulation into a single parameter Λ:

$$\Lambda^2 = \frac{\Gamma^2}{2E}. \tag{21}$$

The stream function ψ is decomposed as

$$\psi = \psi_{\partial\Omega} + \Psi, \tag{22}$$

with $\psi_{\partial\Omega}$ an arbitrary function abiding by similar boundary conditions as the unknown ψ:

$$\psi_{\partial\Omega} = a_q \text{ on } \Omega_q, \quad q \in [0, Q] \tag{23}$$

and Ψ a new unknown which abides by homogeneous Dirichlet boundary conditions: $\Psi = 0$ on the entire boundary $\partial\Omega = \bigcup_{q\in[0,Q]} \Omega_q$. In practice, various simple but regular forms are picked for $\psi_{\partial\Omega}$ but we verify that the final results do not depend on this choice. Without loss of generality, we set $a_0 = 0$ in the following.

More precisely, in the case of a ring domain of respective interior and exterior radii R_1 and R_0, with $\psi_{\partial\Omega} = a_1$ at R_1 and $\psi_{\partial\Omega} = 0$ at R_0, $\psi_{\partial\Omega}$ can be chosen as a function of the distance r from the ring center as

$$\psi_{\partial\Omega}(r) = a_1 \frac{R_0 - r}{R_0 - R_1}. \tag{24}$$

$\Delta\psi_{\partial\Omega}$ is then directly computed regardless of the shape chosen for $\psi_{\partial\Omega}$.

Replacing this decomposition (22) into the fundamental equation of the problem (19) leads to a new version of (19) for the problem on the unknown Ψ:

$$-\Delta\Psi + \beta\Psi = \Delta\psi_{\partial\Omega} - \beta\psi_{\partial\Omega} + \Gamma + \beta(\langle\psi_{\partial\Omega}\rangle + \langle\Psi\rangle). \tag{25}$$

The system to be solved is now (25),(20). We will in a first step obtain the various solutions of the local problem (25), and these will be sorted according to the criterion (20) in a second step in order to obtain the minimum-enstrophy states.

1. The continuous branch

As Ψ satisfies homogeneous Dirichlet boundary conditions, it can be decomposed on the eigenbasis (β_j, e_j) of the Laplacian operator, while enforcing the conditions

$$\Delta e_i = \beta_i e_i, \quad \langle e_i e_j\rangle = \delta_{ij}, \quad e_i|_{\partial\Omega} = 0. \tag{26}$$

The solution ψ and its Laplacian $\Delta\psi$ are decomposed into

$$\psi = \sum_{j=1}^{N} b_j e_j + \psi_{\partial\Omega}, \quad \Delta\psi = \sum_{j=1}^{N} b_j\beta_j e_j + \Delta\psi_{\partial\Omega} \tag{27}$$

with $e_j = 0$ on Ω_0 and Ω_q, $q \in [1, Q]$ and $\psi_{\partial\Omega} = a_q$ on Ω_q, $q \in [1, Q]$. Let $R(\beta, \psi_{\partial\Omega})$ be defined as

$$R(\beta, \psi_{\partial\Omega}) = \Delta\psi_{\partial\Omega} + \beta(\langle\psi_{\partial\Omega}\rangle - \psi_{\partial\Omega}). \tag{28}$$

By injecting (27) into (25) and using the definition (28) for $R(\beta, \psi_{\partial\Omega})$, we obtain

$$\sum_i b_i(\beta - \beta_i)e_i = \Gamma + R(\beta, \psi_{\partial\Omega}) + \beta\langle\Psi\rangle. \tag{29}$$

In order to get a direct expression for the coefficient b_j, the scalar product of relation (29) by the eigenvector e_j is calculated, and the averaging operator $\langle\cdot\rangle$ is applied to the result. Since $\langle e_i e_j\rangle = \delta_{ij}$, we have $\forall j \in [1, N]$ and for $\beta \neq \beta_j$

$$b_j = \frac{\{\langle R(\beta, \psi_{\partial\Omega})e_j\rangle + \Gamma\langle e_j\rangle + \beta\langle e_j\rangle\langle\Psi\rangle\}}{(\beta - \beta_j)}, \tag{30}$$

with the case $\beta \to \beta_j$ being tackled a bit further in the resolution. In a final step, $\langle\Psi\rangle$ is isolated by multiplying relation (30) by $\langle e_j\rangle$, $\forall j \in [1, N]$ and by adding all relations over $j \in [1, N]$. With $\langle\Psi\rangle = \sum_j b_j\langle e_j\rangle$, we get

$$\langle\Psi\rangle = \frac{\sum_j \frac{\langle e_j\rangle}{(\beta-\beta_j)}\{\langle R(\beta, \psi_{\partial\Omega})e_j\rangle + \Gamma\langle e_j\rangle\}}{1 - \beta\sum_j \frac{1}{(\beta-\beta_j)}\langle e_j\rangle^2}. \tag{31}$$

Replacing (31) into (30) leads to a direct expression for each coefficient b_j required to compute Ψ and then ψ based on the circulation Γ, the parameter β, the eigenbasis $(\beta_i, e_i)_{i\in[1,N]}$, and the boundary conditions through the function $\psi_{\partial\Omega}$.

This expression referred to as a *continuous* solution works for any value of β, but a few limit cases can be considered:

(1) If $\beta \to \beta_i$ with $\langle e_i\rangle = 0$, the relations (30) and (31) hold.

(2) If $\beta \to \beta_i$ with $\langle e_i\rangle \neq 0$, both relations (30) and (31) converge to a finite value, but an equivalent expression must be used in the numerical implementation in order to prevent any divergent quantity. The equivalent expression used was

$$b_i \underset{\beta\to\beta_i}{\sim} \frac{\langle R(\beta, \psi_{\partial\Omega})e_i\rangle + \Gamma\langle e_i\rangle}{\beta - \beta_i - \beta\langle e_i\rangle^2}. \tag{32}$$

(3) If $\beta \to \beta_*$, with β_* verifying

$$1 - \beta_* \sum_j \frac{1}{(\beta_* - \beta_j)}\langle e_j\rangle^2 = 0, \tag{33}$$

this is a root of relation (31) leading to a diverging $\langle\Psi\rangle$ and further to a diverging energy. This limit case allows the continuous solution to have $\Lambda \to 0$ despite $\Gamma \neq 0$, and corresponds to a high-energy solution. As detailed by Naso *et al.* [12], it also marks the limit between a "positive" ($\beta > \beta_*$) and "negative" ($\beta < \beta_*$) monopolar state in simple geometries, and it is accompanied by a discontinuity of the chemical potential α.

In summary, the continuous solution is expressed as

$$\psi_{\text{cont}}(\Gamma, \beta, \psi_{\partial\Omega}) = \sum_{j=1}^{N} b_j(\Gamma, \beta, \psi_{\partial\Omega}) e_j + \psi_{\partial\Omega}, \qquad (34)$$

with $b_j(\Gamma, \beta, \psi_{\partial\Omega})$ defined by (30). Note that ψ_{cont} does not formally depend on $\psi_{\partial\Omega}$ but only on the boundary values a_q on $\partial\Omega_q$.

2. The mixed branches

It can be shown that when $\beta = \beta_i$ with β_i an eigenvalue associated with an eigenvector e_i of zero mean $\langle e_i \rangle = 0$, a certain class of solutions coined as *mixed* solutions ψ_{mix} can be linearly constructed as

$$\psi_{\text{mix}}(\Gamma, \beta_i, \psi_{\partial\Omega}) = \psi_{\text{cont}}(\Gamma, \beta_i, \psi_{\partial\Omega}) + \gamma e_i, \quad \forall \gamma \in \mathbf{R}. \qquad (35)$$

These mixed solutions are connected to the family of continuous solutions through the case $\gamma = 0$, and lead to the pure eigenvector e_i when $\gamma \to \pm\infty$. For these solutions, the degree of freedom β is replaced by the parameter γ in (35). As this replacement is quite straightforward in the exploitation of the following phase diagrams, no further distinction will be made between these two parameters.

B. Exploration of the parameter space

1. Calculation of the (β, Λ^2) phase diagram

The point of this resolution being to determine which one of the steady solutions has a lower enstrophy under each possible physical configuration, an exploration of the constraints space (E, Γ) is devised, so as to be able to condense the obtained results in so-called phase diagrams. The aim is to transfer the variations of the constraints on the degrees of freedom in the resolution method, namely, $(\beta, \Gamma, \psi_{\partial\Omega})$ and $(\gamma, \Gamma, \psi_{\partial\Omega})$, respectively, for continuous and mixed solutions. The nonzero boundary condition $\psi_{\partial\Omega}$ represents an additional unknown which can be varied to explore the now larger variety of possible stable states.

While the energy $E = \frac{1}{2}\langle \nabla\psi \cdot \nabla\psi \rangle$ is expressed as a function of the unknown stream function ψ, we also have to account for the boundary terms in our case. As detailed in Appendix A, the proper expression including the circulation around the obstacles Γ_q as well as the a_q boundary conditions on ψ is

$$E = -\frac{1}{2}\beta(\langle \Psi^2 \rangle - \langle \Psi \rangle^2) + \frac{1}{2}\Gamma\langle \Psi \rangle - \frac{1}{2}\sum_{q=1}^{Q} a_q \Gamma_q. \qquad (36)$$

In a first step, the case of constant boundary conditions $\psi_{\partial\Omega}$ is explored for a given value of Γ, and the resulting $(\beta, \Lambda^2)_\Gamma$ phase diagram is plotted. The enstrophy evolves as $\Gamma_2 \propto -\beta$ (see [14,16]), which allows one to compare the enstrophy of the different solutions through their respective position in the diagram: for equal external constraints, the solution associated with the highest value of β has a lower enstrophy. However, different solutions for equal values of the Euler invariants can be stable due to the additional unknown a_q.

The boundary conditions a_q are therefore varied along a certain range, with a computation of the $(\beta, \Lambda^2)_\Gamma$ phase diagram for each boundary conditions combination $(a_q)_{q\in[1,Q]}$. The resulting phase diagrams are then ordered by circulation around the obstacles Γ_q. In the case of a single obstacle, this amounts to plotting $\beta = f(\Lambda^2)$ with Γ_1 as an additional dimension. The resulting database is then interpolated into a hypersurface $\beta = f(\Lambda^2, \Gamma_q, q \in [1, Q])_\Gamma$, in which the least-enstrophy stable solutions verifying (25),(20) can be found.

Sections of this hypersurface can also be taken for given values of each circulation around an obstacle Γ_q, leading to fixed-circulation $(\beta, \Lambda^2)_{\Gamma,\Gamma_q,q\in[1,Q]}$ phase diagrams. In these diagrams, comparing solutions for a fixed value of Λ^2 amounts to setting the constraint on the energy. This allows one to determine the least-enstrophy solution in the chosen set of external constraints (Γ, E) and for given values of $\Gamma_q,\ q \in [1, Q]$).

2. Search of the least-enstrophy solution in the (β, Λ^2) diagram

An interpretation of the (β, Λ^2) diagram helps identifying which solution type has the lowest enstrophy under a given set of Euler invariants values and for given values of $\Gamma_q,\ q \in [1, Q]$). It mostly amounts to a comparison between (1) β^*, the largest root of the continuous solution leading to $\Lambda_{\text{cont}}(\beta^*) = 0$ and (2) β_1, the largest eigenvalue associated with a zero-mean eigenvector, on which the potentially least-enstrophy solution can be built.

Indeed, the continuous solution has a lower enstrophy in the entire parameter range if $\beta^* > \beta_1$ as in the case of the square shown in Appendix C, but a bifurcation can exist between mixed and continuous solutions if $\beta_1 > \beta^*$ as shown in the results for a ring-shaped domain in Sec. IV. In both cases, however, a steady state with $\beta < \beta_1$ is unstable; as demonstrated by Naso *et al.* [12], a perturbation $\delta\omega = \psi_1$ does conserve the constraints of the optimization problem (11) while leading to a negative value for the second-order variations of the functional $J[\psi]$.

We therefore use the aforementioned resolution method to plot the (β, Λ^2) diagram at constant $\Gamma_q,\ q \in [1, Q]$. It will display (1) whether β^* is $<$ or $> \beta_1$, indicating the possibility of two stable regimes and (2) if two stable states can exist, what the critical bifurcation point Λ^2 between them is.

The numerical discretizations used along the resolution are described in Appendix B, and a validation of the resolution method is presented in Appendix C. The results obtained through this procedure for the particular case of a domain with one obstacle ($Q > 1$) are presented next in Sec. IV. Indeed, such a simple annular domain already displays interesting bifurcations between stable states, and the complete $(\beta, \Lambda^2, \Gamma_1)$ 3D surface is still displayable.

IV. CIRCULAR ANNULUS CONFIGURATION

The case of an annular domain geometry is explored in this section; this geometry consists of a circular domain of radius $R_0 = 0.45$ in the center of which a circular obstacle of radius R_1 is placed. Different values of R_1 have been investigated giving similar results. Without loss of generality, we present the case $R_1 = 0.1$.

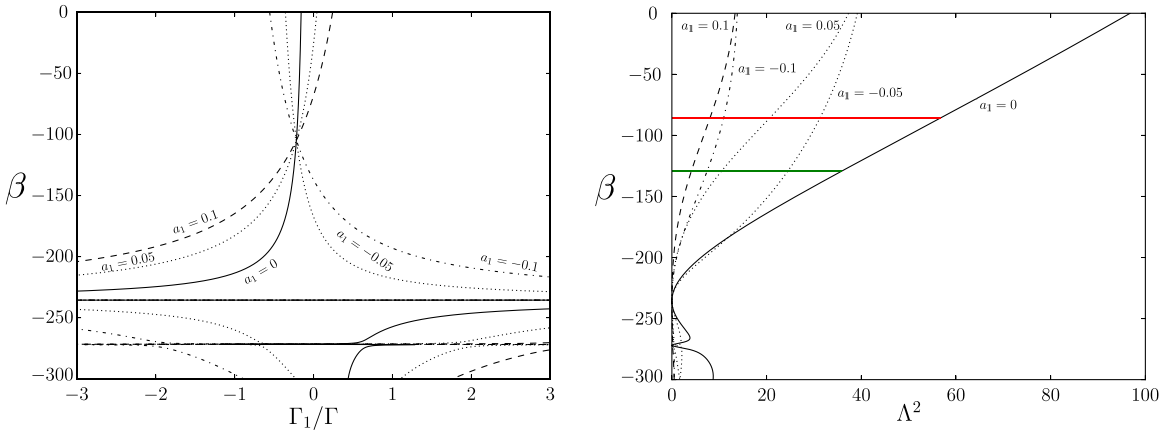

FIG. 3. Representation of MEP solutions in the case of a ring with outer radius $R_0 = 0.45$ and inner radius of $R_1 = 0.1$ at different a_1. The total circulation is set at $\Gamma = 1$. (Left) $(\beta, \Gamma_1/\Gamma)$ plane. (Right) (β, Λ^2) plane.

The full exploitation of the numerical resolution method described in Sec. III allows one, in the case of a one-obstacle annular domain, to respectively draw the ensemble of curves $[\beta = f(\Gamma_1/\Gamma)]_{a_1 \in \mathcal{R}}$ and $[\beta = f(\Lambda^2)]_{a_1 \in \mathcal{R}}$ for different values of a_1. In Fig. 3 the continuous solutions are shown as well as the mixed solutions associated to the first (higher β) and second (lower β) zero-mean eigenvectors.

Several findings can be observed in these two plots:

(1) The circulation around the obstacle Γ_1/Γ of a continuous solution with constant a_1 varies with the energy (through the parameter Λ).

(2) The circulation around the obstacle of a mixed solution is constant with varying γ, which is notably because zero-mean eigenvectors themselves have a zero circulation around the obstacle, and results in the mixed solutions not being visible in the $(\beta, \Gamma_1/\Gamma)$ view in Fig. 3.

(3) The $\beta \to \beta_*$ case, which could be treated continuously in the (β, Λ^2) phase diagrams, now induces a strong divergence in the $(\beta, \Gamma_1/\Gamma, \Lambda^2)$ case. Indeed, as $\beta \to \beta_*$, the continuous solution diverges to a high-energy positive or negative monopolar state, which conveniently leads to $\Lambda \to 0$ in the convex domain case, but here leads to $\Gamma_1/\Gamma \to \pm\infty$ and thus the horizontal lines visible in the $(\beta, \Gamma_1/\Gamma)$ view in Fig. 3.

(4) In the case of inhomogeneous Dirichlet boundary conditions, without taking the circulation Γ_1/Γ into account, several mixed solutions can seem more stable than the continuous solution. However, taking all parameters into account in the following will show that only the mixed solution based on the first zero-mean eigenvector has a lower enstrophy than the continuous solution for given values of Γ_1, and further that the global mininum-enstrophy solution over the entire range of possible Γ_1 is the continuous solution.

(5) A point of interest seems to appear in Fig. 3 around $\beta = -107$ with the convergence of all phase diagrams to a single point, but it must be noted that the continuous solutions observed there do not have equal values of the parameter Λ^2 and thus would not actually converge in a 3D representation of the results.

It is possible to represent $(\beta, \Lambda^2)_{\Gamma_1/\Gamma}$ 2D phase diagrams as shown in Fig. 4 for the example of $\Gamma_1/\Gamma = -0.1$. They amount to a comparison of the solutions for a given value of the circulation around the obstacle. This phase diagram confirms that a bifurcation is possible in the case of an annular domain between mixed and continuous solutions for different values of Λ^2. The first mixed solution and the continuous solutions have, respectively, a lower enstrophy in the ranges $\Lambda^2 < \Lambda^2_{\text{bif}}$ and $\Lambda^2 > \Lambda^2_{\text{bif}}$. Significantly, this observation holds for any value of the circulation around the obstacle; regardless of the value picked in the interpolation for Γ_1/Γ, a lower-enstrophy zone persists for the mixed solution. This means that in our set of hypotheses and for given values of the circulation Γ_1 around the obstacle, the system should always select a two-vortices state over a monopolar one, provided it contains enough kinetic energy at fixed total circulation. However, the criterion (20) needs to be taken into account to obtain the global least-enstrophy stable states.

Therefore, the results are ordered into a "stability map," showing the stability zones of each category of solution in the parameter space. This representation is shown in Fig. 5,

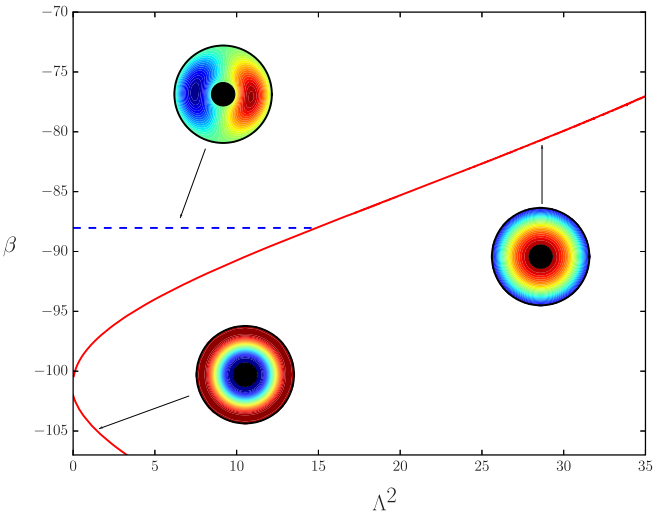

FIG. 4. Interpolated $(\beta, \Lambda^2)_{\Gamma_1/\Gamma}$ phase diagram in the case of an annular domain with a central obstacle, for $\Gamma_1/\Gamma = -0.1$. The curved solid line corresponds to the continuous solution and the horizontal dashed line to the mixed solution associated with the first zero-mean eigenvector.

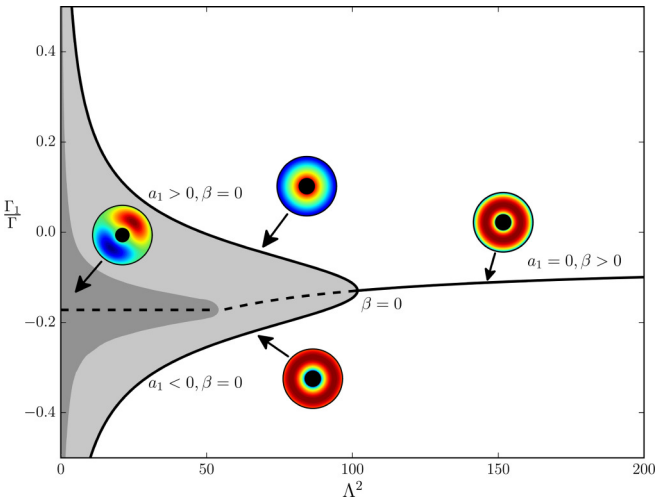

FIG. 5. Bifurcation diagram showing the domination zones of the "mixed" (dark gray) and "continuous" (light gray) solutions in parameter space, in the case of the annular domain. It was obtained by scanning E and Γ_1/Γ values while keeping Γ constant. The global minimum of the enstrophy is obtained through $\beta a_1 = 0$ and is shown as a thick black curve.

and it amounts to viewing the combination of the line plots shown in Fig. 3 from "above," and only observing the highest-β solution for each point in the $(\Lambda^2, \Gamma_1/\Gamma)$ plane. The zone of prevalence for the mixed solutions is displayed in dark gray in Fig. 5 while the zone for the continuous solutions is shown in light gray. Additionally, the overall minimum value for the enstrophy is displayed as a thick black curve.

For inhomogeneous boundary conditions, the overall minimum is reached with $\beta = 0$. In this case, we obtain $-\langle \Delta\psi \rangle = \Gamma$ from (19) and thus $\Gamma_2 = \frac{1}{2}\langle \Gamma^2 \rangle$ from (7). Notably, both the stable branches observed in Fig. 5 for $\beta = 0$ have the same enstrophy.

When restricting $a_1 = 0$, the stable solution is found for $\beta > 0$ along the curve in Fig. 5 with $\Lambda^2 \geqslant 100$. The point $\beta = 0$, $a_1 = 0$ joining the two regimes is a continuous bifurcation point between a single stable state ($\Lambda^2 > 100$) and a pair of possible stable states ($\Lambda^2 < 100$) that differ by the sign of a_1.

Furthermore, this plotting method particularly highlights the fact that the stability zone of the mixed solution is of maximal amplitude for a particular value of $\Gamma_1/\Gamma \simeq 0.2$ in the case of $\Gamma = 1$. This result can be interpreted as the best repartition of the total circulation Γ between the internal and external boundaries so as to foster a dipolar fluid state.

Several key findings can be drawn from this numerical study of the minimal enstrophy states in a domain with an obstacle based on the MEP.

(1) As in the case of an empty disk, lower-enstrophy zones have been identified for both the mixed and continuous solutions in the geometries of a square and a circle with a central obstacle for given values of the circulation Γ_1 around the obstacle.

(2) Either $\beta = 0$ or $a_1 = 0$, $\beta > 0$ lead to the overall minimal enstrophy states corresponding to the continuous solution, but these can only be found when exploring the range of possible circulations Γ_1 using inhomogeneous Dirichlet boundary conditions.

(3) A bifurcation point exists at $\beta = 0$, $a_1 = 0$; it separates a single, low-energy branch (high Λ) from two high-energy branches (small Λ) with opposed a_1 leading to opposite circulations around obstacle Γ_1/Γ.

It can also be noted that the two solution types identified in Fig. 5 can be related to the two flow regimes identified in a 2D rotating-ring flow experiment (for instance, [27]). Indeed, the flow regimes identified therein consist of

(1) A "zonal" flow regime with a dominant central vortex around the obstacle, reminiscent of the single vortex continuous solution.

(2) A "blocked" flow regime characterized by a loss of rotational symmetry and the emergence of opposed counter-rotating vortices on each side of the obstacle, which could correspond to a mixed solution from our results.

Although only a limited qualitative comparison can be drawn at this point between the mixed or continuous solutions and the zonal or blocked flow regime in a ring-shaped domain geometry, it is noteworthy that the resolution method described here can prove of interest in a numerical study of this phenomenon based on MEP-based statistical physics.

It is notable that this layout of the stable states in the parameter space for a ring domain geometry, namely, the sole existence of one- or two-vortices solutions, holds for any size of the central obstacle in our numerical results. Although this result is counter-intuitive, as one could expect a progressive split of the stable states into multiple-vortices solutions as the domain is increasingly thin, it is a consequence of the hypotheses chosen in this approach, which favor the largest-scale states as a consequence of the inverse cascade process. The analytical results mentioned in Appendix C 2 confirm this analysis, as the eigenvalues respectively associated to four-, six-, and eight-vortices zero-mean eigenvectors are inferior to that associated to the two-vortices one for any value of the central obstacle radius.

V. MULTIPLE OBSTACLES CONFIGURATION

In this section, we apply the resolution method for the MEP applied to a multiple obstacle configuration relevant to PWR rod-bundle flows.

A. Description of the case

As already mentioned, a supplementary variable is added to the problem for each obstacle inside the computational domain through the different circulations Γ_q. Here we consider the case of a square domain with two obstacles placed in opposite corners mimicking basic features of rod-bundle flow configurations, as depicted in Fig. 2. The following example not only aims at being a proof of concept of our method in a domain with multiple obstacles but also to understand possible bifurcations occurring in PWR experiments.

B. Results

We reduce the degree of freedom of the problem by using the mirror symmetry along the diagonal existing also in rod-bundle flow experiments. Thus, we impose $a_1 = a_2$ leading to equal circulations around the two obstacles $\Gamma_1 = \Gamma_2$ regardless of the total energy and circulation. This allows

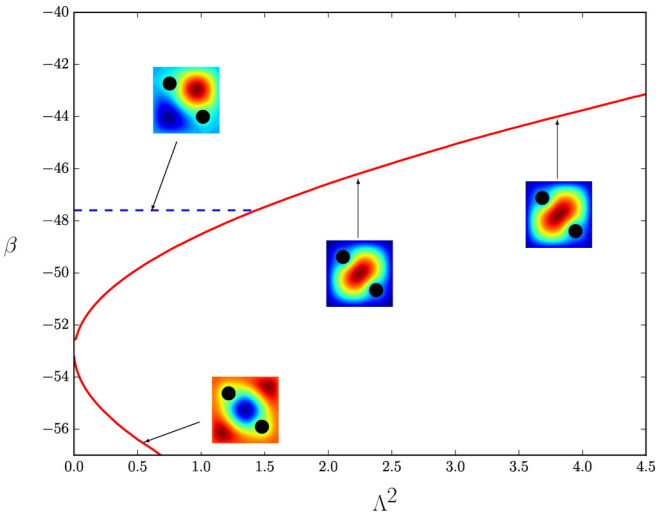

FIG. 6. Interpolated $(\beta, \Lambda^2)_{\Gamma_1}$ phase diagram in the case of a square domain with two opposed obstacles and identical circulations. Here $\Gamma_1 = \Gamma_2 = 0.1$. The curved and horizontal lines respectively correspond to the continuous solution and the mixed solution associated with the first zero-mean eigenvector.

a simplified exploration of the parameter space despite the additional complexity of the geometry.

The $(\beta, \Lambda^2)_{\Gamma_1}$ interpolated diagram is shown for $\Gamma_1 = \Gamma_2 = 0.1$ in Fig. 6. A bifurcation is visible therein between the continuous and mixed solutions. Interestingly, the continuous solution features a single vortex distorted along the diagonal without obstacles, while the first mixed solution displays two opposed vortices with a separation line along the diagonal with the obstacles.

The interpolated stability map for $\Gamma_1 = \Gamma_2 = 0.1$ with $\Gamma = 1$ is shown in Fig. 7. For a fixed value of Γ_1, a bifurcation

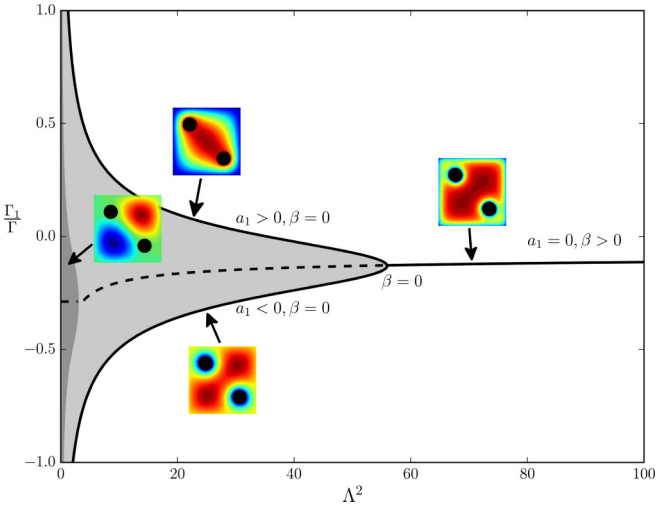

FIG. 7. Bifurcation diagram showing the domination zones of the "mixed" (dark gray) and "continuous" (light gray) solutions in parameter space, in the case of a square domain with two obstacles of equal circulation. It was obtained by scanning E and Γ_1 values while keeping Γ constant. The global minimum of the enstrophy is obtained through $\beta a_1 = 0$ and is shown as a thick black curve.

is observable between a monopolar continuous solution and a dipolar mixed solution (respectively, light- and dark-gray zones in Fig. 7). Similarly to the case of the annular domain, relaxing the conservation of Γ_1 through either $\beta = 0$ or $a_1 = 0$, $\beta > 0$ leads to the overall minimal enstrophy states displayed as a thick black curve in Fig. 7.

C. Discussion

The results shown in Figs. 6 and 7, namely, the existence of bifurcations between mixed and continuous solutions and between the single and double minimum-enstrophy branches, can actually be of particular interest to the field of PWR rod-bundle flows. As mentioned previously, these three-dimensional flows tend to develop coherent structures in their 2D cross section which we aim to study using a Taylor "frozen turbulence" hypothesis. The shape of these structures is initially determined by arrays of small vanes placed between rods in so-called mixing grids. However, spontaneous reorganizations of the cross-section flow were observed in some rod-bundle experiments and numerical simulations [18]. Such a reorganization, only observed in experiments but not reproduced in simulations nor fully understood at this point, amounts to a 90° rotation of the cross-section flow from a mostly 45° angle to a 135° alignment, as illustrated in Fig. 2 from Bieder *et al.* [18].

The stable solutions shown in Fig. 7 in a simplified domain geometry can be related to this phenomenon. Indeed, both the single solution for $\Lambda^2 > \Lambda^2_{\text{bif}} \simeq 55$ and the lower branch for $\Lambda^2 < \Lambda^2_{\text{bif}}$ display an alignment with the 45° diagonal of the square domain. On the other hand, the upper branch $(\Gamma_1/\Gamma > -0.2)$ features a vortex around the two obstacles and aligned with the 135° diagonal. To a lesser extent due to their higher enstrophy, the bifurcation between continuous and mixed solutions in Fig. 6 display a 90° rotation as well.

In a real flow with imperfect conservation of the invariants considered in our resolution, one could envision an evolution of Λ in the (β, Λ^2) diagram shown in Fig. 7 so that the stable steady solution shifts from one solution type to the other, effectively leading to a rotation of the flow. These results hint at a possibly similar situation in the case of the 5×5 cylinder array described in [18]; the initial diagonal flow could be imposed by alternating rotations around each obstacle. Further along the 3D axial distance from the mixing grid, and further in time within the Taylor hypothesis, declining integral quantities due to dissipation could modify the Λ parameter, leading to a phase transition from a solution type to another and effectively inducing a 90° rotation of the flow. Naturally, these considerations are only qualitative at this point, but they should prove a first step in the effective use of such statistical resolution methods in the study of flows around obstacles such as PWR rod-bundle flows.

VI. CONCLUSION

In this study, we present and apply the MEP to domain geometries containing inner obstacles relevant for pressurized-water reactors rod-bundle flows. The resolution of the variational problem is adapted so as to enable different values of the stream function around each separate piece of boundary.

An explicit expression for the solutions based on a given set of parameters is derived, and the methodology developed to recover the stable steady solution for each given set of Euler constraints is detailed. This sheds light on new bifurcation mechanisms occurring in such flows.

We first apply this resolution method to the case of an annulus domain, and then identify the parameters in a phase diagram allowing one or two vortices corresponding to the continuous or mixed solution branches as in the classical MEP problem without obstacles. However, it is shown that the circulation Γ_1 around the inner boundary is fully determined above a critical value for Λ, the circulation divided by square root of kinetic energy. Below this threshold, solutions with various circulations Γ_1 are allowed and surprisingly with different signs. Interestingly, this suggests that flows in annular geometries and starting from close initial conditions can evolve very differently with opposite circulations around the central boundary.

Then we turn our attention to the case of a square geometry with two diagonally opposed obstacles, as a paradigm of flow phenomenologies around multiple obstacles. Within this framework, we propose to reduce the degrees of freedom of this problem by considering a symmetrical configuration with equal circulations around the different inner boundaries. This case appears particularly striking as it involves qualitatively a 90° rotation of the flow. The solutions can indeed experience a transition from a single vortex, distorted along the diagonal without obstacles, to a dipolar state symmetrical about the diagonal with obstacles. This phenomenology clearly recalls the observations in PWR rod-bundle flow experiments.

Accordingly, the feasibility of an algorithmic solver returning the most probable steady solutions within complex geometries for a given set of Euler invariants is demonstrated. One could also foresee the adaptation of this method to consider other dynamical stability criteria than the MEP, typically in order to consider the conservation of higher moments of the vorticity in cases of truly inviscid flows.

Further work is currently under way to use the resolution method described here in domain geometries closer to cross sections of rod-bundle flows, and to further this study through 3D and 2D computational fluid dynamics simulations.

APPENDIX A: EXPRESSION OF THE ENERGY

The expression of the kinetic energy has to be modified, so as to take into account the new boundary conditions on the stream function ψ. Starting from the general expression for the energy based on the flow velocity $\mathbf{u} = (u_x, u_y)$:

$$E = \int_\Omega \frac{\mathbf{u}^2}{2}\, d\mathbf{r} = \frac{1}{2}\int_\Omega \left[\left(\frac{\partial\psi}{\partial y}\right)^2 + \left(\frac{\partial\psi}{\partial x}\right)^2\right] d\mathbf{r}, \quad \text{(A1)}$$

which gives

$$E = \frac{1}{2}\int_\Omega (\nabla\psi)^2\, d\mathbf{r}. \quad \text{(A2)}$$

Using the decomposition $\psi = \psi_{\partial\Omega} + \Psi$ in (A7), with $\Psi = 0$ a $\partial\Omega$ zero Dirichlet boundary condition and $\psi_{\partial\Omega}$ an arbitrary function linearly evolving between the a_q boundary conditions set on ψ on each piece of boundary Ω_q:

$$E = \frac{1}{2}\int_\Omega [\nabla(\psi_{\partial\Omega} + \Psi)\cdot\nabla(\psi_{\partial\Omega} + \Psi)]\, d\mathbf{r}. \quad \text{(A3)}$$

An integration by parts is used, producing the following expression for the energy:

$$E = \frac{1}{2}\int_\Omega [\Delta(\psi_{\partial\Omega} + \Psi)(\psi_{\partial\Omega} + \Psi)]\, d\mathbf{r} - \frac{1}{2}\int_{\partial\Omega} [\nabla(\psi_{\partial\Omega} + \Psi)(\psi_{\partial\Omega} + \Psi)]\cdot\mathbf{n}\, d\mathbf{l}. \quad \text{(A4)}$$

Since $\langle\cdot\rangle \equiv \int_\Omega \cdot\, d\mathbf{r}$ and using the fundamental equation (25) to express $\Delta(\psi_{\partial\Omega} + \Psi)$ in terms of Γ, β and $\langle\psi_{\partial\Omega} + \Psi\rangle$:

$$\frac{1}{2}\int_\Omega [\Delta(\psi_{\partial\Omega} + \Psi)(\psi_{\partial\Omega} + \Psi)]\, d\mathbf{r} = -\frac{1}{2}\beta(\langle(\psi_{\partial\Omega}+\Psi)^2\rangle - \langle\psi_{\partial\Omega} + \Psi\rangle^2) + \frac{1}{2}\Gamma\langle\psi_{\partial\Omega} + \Psi\rangle. \quad \text{(A5)}$$

Knowing that $\Psi = 0$ on $\partial\Omega$ while $\psi_{\partial\Omega} = 0$ on Ω_0 and $\psi_{\partial\Omega} = a_q$ on Ω_q for $q \neq 0$:

$$\begin{aligned}\frac{1}{2}\int_{\partial\Omega} [\nabla(\psi_{\partial\Omega} + \Psi)(\psi_{\partial\Omega} + \Psi)]\cdot\mathbf{n}\, d\mathbf{l} &= \frac{1}{2}\sum_q a_q \int_{\partial\Omega_q} [\nabla(\psi_{\partial\Omega} + \Psi)]\cdot\mathbf{n}\, d\mathbf{l} \\ &= \frac{1}{2}\sum_q a_q\Gamma_q \end{aligned} \quad \text{(A6)}$$

with Γ_q the circulation of the flow along each piece of boundary Ω_q.

The final expression of the energy is thus

$$E = -\frac{1}{2}\beta(\langle\psi^2\rangle - \langle\psi\rangle^2) + \frac{1}{2}\Gamma\langle\psi\rangle - \frac{1}{2}\sum_q a_q\Gamma_q. \quad \text{(A7)}$$

APPENDIX B: NUMERICAL DISCRETIZATIONS

The following results were obtained through a discretized calculation tool based on a finite differences method. Computations were performed on a 2D Cartesian mesh with adequate normalizations based on the domain surface area. Expressions (25), (30), and (31) were projected on all interior nodes of the domain, with the value of the unknown ψ being set by the boundary conditions through $\psi_{\partial\Omega}$ on the boundary nodes.

A five-point stencil discretization was used for the Laplace operator, namely, if $\psi_{i,j}$ is the value of ψ at coordinates (i, j) in the mesh and h is the mesh spatial step,

$$\Delta\psi_{i,j} = \frac{\psi_{i+1,j} + \psi_{i-1,j} + \psi_{i,j+1} + \psi_{i,j-1} - 4\psi_{i,j}}{h^2}. \quad \text{(B1)}$$

As a consequence, the zero Dirichlet boundary condition set on the Laplace operator was enforced through a modification of expression (B1) on nodes in the vicinity of the boundary. On such a node (i, j) next to a boundary node

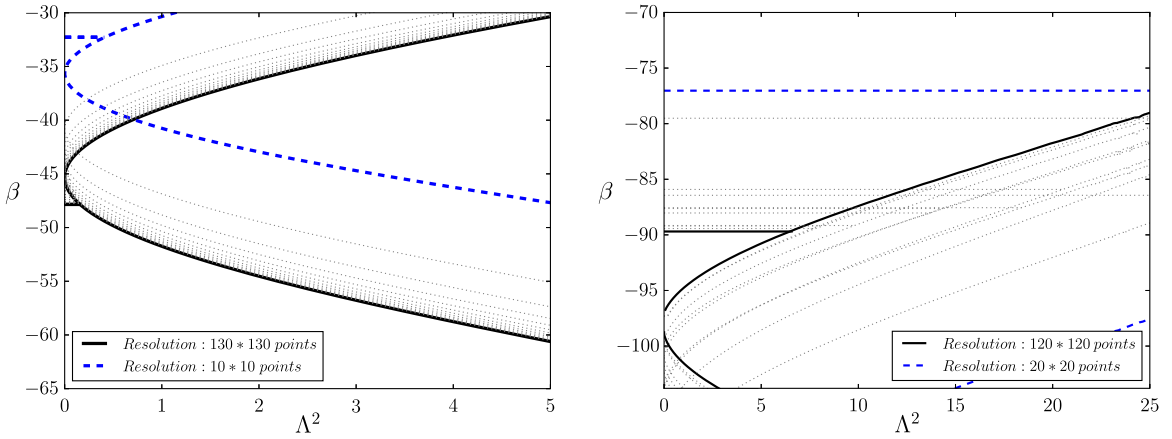

FIG. 8. Mesh convergence of the phase diagram of the continuous and mixed solution in the case of a square domain geometry (left) and annular domain geometry (right). The dashed, dotted, and solid lines, respectively, correspond to lowest, intermediary, and highest mesh resolutions.

$(i+1, j)$, $\Delta\psi_{i,j}$ would be implemented as

$$\Delta\psi_{i,j} = \frac{\psi_{i-1,j} + \psi_{i,j+1} + \psi_{i,j-1} - 4\psi_{i,j}}{h^2}. \tag{B2}$$

A first-order central difference was used for the gradient operator $\boldsymbol{\nabla}$ along each direction

$$\nabla_i \psi_{i,j} = \frac{\psi_{i+1,j} - \psi_{i-1,j}}{2h}. \tag{B3}$$

The spatial resolutions required to ensure sufficient convergence of the results are discussed in Appendix C 1.

APPENDIX C: METHOD VALIDATION

1. Mesh convergence and robustness of the results

Several tests were performed on the validity of the numerical resolution, namely, convergence of the phase diagrams and computed quantities such as the circulation around each obstacle Γ_q with mesh refinement, as well as robustness of the results with respect to small fluctuations in the input data.

The mesh convergence of the phase diagram in the case of a square domain geometry is shown in Fig. 8, for resolutions from $10 * 10$ to $130 * 130$ points. A mesh resolution of $100 * 100$ points was required for the results to be within 1% of their converged value. Similarly, the mesh convergence of the interpolated phase diagram in an annular domain geometry is also shown in Fig. 8, for resolutions from $20 * 20$ to $120 * 120$ points. A resolution of $100 * 100$ points was required here as well for the results to be within 1% of their converged value.

Small variations of the domain shape (aspect ratio, obstacle position, and size) and of the input parameters (total circulation and boundary conditions a_q) were found to have limited to no impact on the results, showing the robustness of the method.

2. Comparison to analytical results

In the case of a ring domain geometry, a validation is possible through an analytical approach by obtaining the eigenvalues β_i of the Laplace operator. An eigenvector $\psi_i(R, \theta)$ associated to the eigenvalue β_i and expressed here in polar coordinates verifies the equation

$$\Delta\psi_i = \partial_{RR}\psi_i + \frac{1}{R}\partial_R\psi_i + \frac{1}{R^2}\partial_{\theta\theta}\psi_i = \beta_i\psi_i, \tag{C1}$$

with $\psi_i(R_0, \theta) = \psi_i(R_1, \theta) = 0$. The unknown is decomposed as

$$\psi_i(R, \theta) = e^{im\theta} f_m(r, \theta), \tag{C2}$$

with $r = R/R_0$ and $m \in \mathbb{N}$, which translates to the equation on f_m

$$\partial_{rr} f_m + \frac{1}{r}\partial_r f_m + \left(\lambda^2 - \frac{m^2}{r^2}\right) f_m = 0, \tag{C3}$$

with $f_m(1, \theta) = f_m(R_1/R_0, \theta) = 0$ and $\lambda^2 = -\beta_i R_0^2$. The general solution of this equation is a combination of Bessel functions of first and second kinds (see Abramowitz and Segun [28]). We impose the Dirichlet boundary condition on the outer radius R_1 to obtain

$$f_m(r) = A\left(J_m(\lambda r) - \frac{J_m(\lambda)}{Y_m(\lambda)} Y_m(\lambda r)\right), \tag{C4}$$

with $A \in \mathbb{R}$. The possible values of λ and subsequently of the possible eigenvalues β_i are obtained through the imposition of the inner boundary condition. For a given value of r_i, we seek to find the zeros of the function

$$h_{r_i,m}(\lambda) = J_m(\lambda r_i) Y_m(\lambda) - J_m(\lambda) Y_m(\lambda r_i). \tag{C5}$$

In a test example for an annular domain geometry with outer radius $R_0 = 0.45$ and inner radius $R_1 = 0.1$, the largest eigenvalues of the Laplace operator were found at $\beta_0 \simeq -72$, $\beta_1 \simeq -88$, and $\beta_2 \simeq -132$. The root of function $h_{r_i=0.1,m=1}$, which corresponds to β_1 as the first eigenvalue associated to a zero-mean eigenvector, was evaluated at $\lambda \simeq -80$. A difference of around 9% is noted between these two values for the annular domain. A much better agreement was obtained between numerical and theoretical eigenvalues in the square domain: $\beta_1 \simeq -47.8$ from our numerical resolution, $\beta_1 \simeq -49.3$ from Naso *et al.* [12]. The larger difference in the annular domain is attributed to the rough treatment of the boundary, which could be improved by replacing the Cartesian grid by a curvilinear

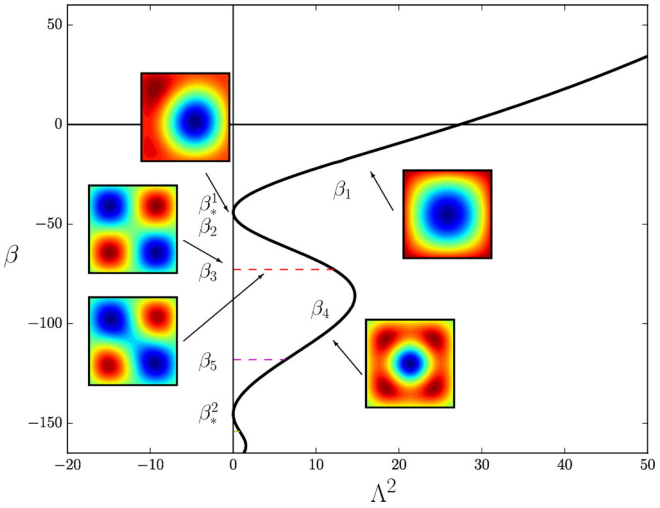

FIG. 9. Phase diagram obtained in a square geometry using our numerical resolution method.

one, for example. We nevertheless considered the numerical results sufficiently close to the analytical ones for a discussion of the results in Secs. IV and V.

3. Recovery of literature results

As a first step, the resolution method previously explained is applied to that of a square geometry with homogeneous Dirichlet boundary conditions. Taking $\psi_{\partial\Omega} = 0$ in this resolution amounts to following the same procedure as detailed by Chavanis *et al.* [14], which allows one to test the validity of the numerical part of the resolution.

The (β, Λ^2) phase diagram we obtained using our numerical resolution method in the case of a square domain is shown in Fig. 9. These results are to be compared with those obtained through an analytical method by Chavanis *et al.* [14] and shown in Fig. 3 therein; the analytical results are correctly recovered.

[1] B. Turkington, A. Majda, K. Haven, and M. DiBattista, Proc. Natl. Acad. Sci. USA **98**, 12346 (2001).
[2] M. J. Schmeits and H. A. Dijkstra, J. Phys. Oceanogr. **31**, 3435 (2001).
[3] L. Onsager, Nuovo Cimento **6**, 279 (1949).
[4] G. Joyce and D. Montgomery, J. Plasma Phys. **10**, 107 (1973).
[5] R. H. Kraichnan, J. Fluid Mech. **67**, 155 (1975).
[6] R. Salmon, G. Holloway, and M. C. Hendershott, J. Fluid Mech. **75**, 691 (1976).
[7] J. Miller, Phys. Rev. Lett. **65**, 2137 (1990).
[8] R. Robert and J. Sommeria, J. Fluid Mech. **229**, 291 (1991).
[9] F. P. Bretherton and D. B. Haidvogel, J. Fluid Mech. **78**, 129 (1976).
[10] W. H. Matthaeus and D. Montgomery, Ann. N.Y. Acad. Sci. **357**, 203 (1980).
[11] C. E. Leith, Phys. Fluids **27**, 1388 (1984).
[12] A. Naso, P. H. Chavanis, and B. Dubrulle, Eur. Phys. J. B **77**, 187 (2010).
[13] A. Naso, P. H. Chavanis, and B. Dubrulle, Eur. Phys. J. B **80**, 493 (2011).
[14] P. H. Chavanis and J. Sommeria, J. Fluid Mech. **314**, 267 (1996).
[15] R. S. Ellis, K. Haven, and B. Turkington, Nonlinearity **15**, 239 (2002).
[16] P. H. Chavanis, Eur. Phys. J. B **70**, 73 (2009).
[17] F. Bouchet, Phys. D: Nonlinear Phenom. **237**, 1976 (2008).
[18] U. Bieder, F. Falk, and G. Fauchet, Prog. Nucl. Energy **75**, 15 (2014).
[19] Y. Fen Shen, Z. Dong Cao, and Q. Gang Lu, Nucl. Eng. Des. **125**, 111 (1991).
[20] M. Corvellec, Phase transitions in two-dimensional and geophysical turbulence, Ph.D. thesis, École Normale Supérieure de Lyon, 2012.
[21] P. Chen and M. C. Cross, Phys. Rev. E **50**, 2022 (1994).
[22] L. Kelvin, Philos. Mag. **24**, 188 (1887).
[23] V. I. Arnol'd, Izv. Vyssh. Uchebn. Zaved. Mat., 3 (1966).
[24] H. Brands, P. H. Chavanis, R. Pasmanter, and J. Sommeria, Phys. Fluids **11**, 3465 (1999).
[25] P.-H. Chavanis, Phys. D: Nonlinear Phenom. **237**, 1998 (2008).
[26] P.-H. Chavanis, A. Naso, and B. Dubrulle, Eur. Phys. J. B **77**, 167 (2010).
[27] Y. Tian, E. R. Weeks, K. Ide, J. S. Urbach, C. N. Baroud, M. Ghil, and H. L. Swinney, J. Fluid Mech. **438**, 129 (2001).
[28] M. Abramowitz and I. A. Stegun, *Handbook of Mathematical Functions: With Formulas, Graphs, and Mathematical Tables* (Courier Corporation, Chelmsford, MA, 1964), Vol. 55.